

A Bayesian 3D Multi-view Multi-object Tracking Filter

Jonah Ong, Ba-Tuong Vo, Ba-Ngu Vo, Du Yong Kim and Sven Nordholm

Abstract—This paper proposes an online multi-camera multi-object tracker that only requires monocular detector training, independent of the multi-camera configurations, allowing seamless extension/deletion of cameras without (retraining) effort. The proposed algorithm has a linear complexity in the total number of detections across the cameras, and hence scales gracefully with the number of cameras. It operates in 3D world frame, and provides 3D trajectory estimates of the objects. The key innovation is a high fidelity yet tractable 3D occlusion model, amenable to optimal Bayesian multi-view multi-object filtering, which seamlessly integrates, into a single Bayesian recursion, the sub-tasks of track management, state estimation, clutter rejection, and occlusion/mis-detection handling. The proposed algorithm is evaluated on the latest WILDTRACKS dataset, and demonstrated to work in very crowded scenes on a new dataset.

Index Terms—Multi-view, Multi-sensor, Visual Tracking, Occlusion Handling



1 INTRODUCTION

THE interest of visual tracking is to jointly estimate an unknown time-varying number of object trajectories from a stream of images [1], [2]. The challenges of visual tracking are the random appearance/disappearance of the objects, false positives/negatives, and data association uncertainty [3]. Multiple object tracking (MOT) algorithms can operate online to produce current estimates as data arrives, or in batch which delay the estimation until further data is available [4]. In principle, batch algorithms are more accurate than online as they allow better data integration into the estimates [3], [5], [6], [7], [8]. Online algorithms, however, tend to be faster and hence better suited for time-critical applications [4], [9], [10], [11].

The common sub-tasks, traditionally performed by separate modules in a MOT system are track management, state estimation, clutter rejection, and occlusion/mis-detection handling. Track management involves the initiation, termination and identification of trajectories of individual objects, while state estimation is concerned with determining the state vectors of the trajectories. Problems such as track loss, track fragmentation and identity switching are caused by false negatives that can arise from occlusions when objects of interest are visually blocked from a sensor, or from mis-detections when the sensor/detector fails to register objects of interest. On the other hand, false positives can lead to false tracks and identity switching. Hence, occlusion/mis-detection handling and clutter rejection are critical for improving tracking performance.

While occlusion handling is just as challenging compared with the other sub-tasks, theoretical developments are

far and few [12]. This is due mainly to the complex object-to-object and object-to-background relationships, as well as computational tractability because, theoretically, all possible partitions of the set of objects need to be considered [4]. In a single-view setting, useful *a priori* information about the objects of interest are exploited to resolve occlusions [3], [5], [11]. However, there are fundamental limitations on what can be achieved with single-view data. In contrast, a multi-view setting naturally allows exploiting complementary information from the data to resolve occlusions since an object occluded in one view may not be occluded in another [13]. Furthermore, from an information theoretic standpoint, data from diverse views will reduce the uncertainty on the set of objects of interest, thereby improving overall tracking performance. Given the proliferation of cameras in today's world, it is imperative to develop effective means for making the best of the information-rich multi-view data sources, not only for occlusion handling, but ultimately to achieve better visual tracking.

The perennial challenge in multi-view visual tracking is the high-dimensional data association problem between the detections and objects, across different views/cameras [12], [14]. So far, a number of batch solutions have been proposed based on: generative modeling and dynamic programming [14]; convolutional neural network (CNN) multi-camera detection (MCD), trained on multi-view datasets [15], followed by track management [16]; and MCD via multi-view CNN training combined with Conditional Random Fields (CRF) models to exploit multi-camera geometry (followed by track management) [17]. These MCD based MOT solutions, which produce trajectories on the ground plane, have been shown to out-perform previous works [15], and demonstrated remarkable performance in crowded scenarios [17]. Note that such data-centric MCDs require retraining when the multi-camera system is extended/reconfigured, and that training/learning is expensive as the input space is very high-dimensional due to the large number of possible combinations across the cameras [18]. In practice, it is desirable for a multi-view MOT system to produce trajectories in 3D world

- J. Ong, B.T. Vo, B.N. Vo, and S. Nordholm are with the Department of Electrical and Computer Engineering, Curtin University, Bentley, WA 6102, Australia.
E-mail: {j.ong1, ba-tuong.vo, ba-ngu.vo, s.nordholm}@curtin.edu.au
- D.Y. Kim is with the School of Engineering, RMIT University, Melbourne, Australia.
E-mail: duyong.kim@rmit.edu.au

frame, online, and requires no retraining for multi-camera extension/reconfiguration (including camera failures) so as to operate uninterrupted.

This paper proposes a model-centric online approach to multi-view MOT that only requires monocular detector training, independent of the multi-camera configurations. Hence, no retraining is needed when the multi-camera system is extended/reconfigured. More importantly, our algorithm has a linear complexity in the total number of detections, thereby scales gracefully with the number of cameras. In addition, by exploiting multi-camera geometry, the algorithm intrinsically operates in 3D world frame, allowing it to track people jumping and falling, suitable for applications such as sports analytics, age care, school environment monitoring, etc. The key innovation is a high fidelity yet tractable 3D occlusion model, amenable to optimal Bayesian multi-sensor multi-object filtering [19], which seamlessly integrates, into a single Bayesian recursion, the sub-tasks of track management, state estimation, clutter rejection, and occlusion/mis-detection handling. We validate our proposed method on the latest WILDTRACKS dataset on ground plane and show comparable results with Deep-Occlusion+KSP+ptrack [16]. To evaluate tracking performance in 3D world frame, we develop a new dataset with varying degrees of difficulties on scenarios with very closely spaced people, with addition/deletion of cameras during operation, and with people jumping and falling.

2 RELATED WORK

Deep Convolutional Neural Networks (CNN) trained on large-scale high-resolution image dataset has been shown to outperform all previous object detectors, including the Aggregated Channel Features (ACF) object detector [20]. Additionally, region proposals with CNN features (R-CNN) have been introduced to increase computational speed in [21], [22]. The common issue in these techniques is the slow training and detection speed. While Faster R-CNN [22], has shown better test-time speed and detection accuracy than its predecessors, it only achieves real-time detection at 5 frames-per-second (fps). Recently, the You Only Look Once (YOLO) real-time object detector, which attains 40fps at mAP of 76.8% (resolution of 544x544) on PASCAL VOC 2007, has gained immense popularity [23]. Its impressive speed is achieved by only scanning the image once, unlike the aforementioned techniques that rely on a sliding classifier for every image. Additionally, spatial constraints, introduced to eliminate unlikely bounding boxes (created over the entire image), allow trade-offs between speed and accuracy via a suitable score threshold [24]. The YOLO detector can also be extended to 3D [25]. The main drawback in this framework is the inability to detect small objects due to the imposed spatial constraints [24].

Progress in object detections facilitated the development of many tracking-by-detection approaches to MOT that typically join the detections together to form consistent trajectories [9], [26], [27]. Tracking-by-detection can be designed for batch or online operations. Online algorithms tend to be faster and better suited for time-critical applications, but may be prone to irrevocable errors if objects are undetected in several frames or if detections at different times are

incorrectly joined [3]. Such errors can be reduced by global trajectory optimization over batches of frames [3], [5], [6], [7], [8]. However, track loss and fragmentation can still be caused by occlusion, which is an active area of research in itself [26]. In single-view/monocular settings, a popular approach to occlusion handling is to exploit *a priori* knowledge of the scene [3], [5], [6].

In a multi-view setting, complementary information from the data can be exploited to resolve occlusions naturally, since an object occluded in one view may not be occluded in another view [13]. One simple approach is to pre-process images from individual views (e.g. via background subtraction) from which occupancy (on the ground plane) can be estimated using Probability of Occupancy Map (POM) [14]. A more sophisticated approach was proposed in [12], which combines multi-view Bayesian network modeling of occlusion relationship and homography correspondence, across all views, with height-adaptive projection (HAP) to obtain final ground plane detections [12].

So far, the best multi-view tracking solution is based on a multi-camera detection (MCD) architecture that uses CNN to train multi-view detectors from monocular and multi-view data [15], together with batch processing to compute global trajectories on the ground plane [16]. Combined with Conditional Random Field (CRF) modeling and Mean Field variational inference, this approach achieves remarkable performance in crowded scenario [17]. This approach is more data-centric than model-centric as the multi-camera detection relies mostly on training from data. Hence, large training sets are required, and the learning algorithm tends to be computationally expensive in exploring tight convergence levels especially for high dimensional scenarios (e.g. large number of cameras) [18].

In practice, it is desirable to have online algorithms whose complexity scale linearly with the number of cameras, and does not require multi-view training so that re-configuration (including addition and deletion) of cameras can be performed without interruption to the operation. Moreover, in a multi-view context, it is more prudent to have trajectories in 3D world frame for applications such as sports analytics, age care, school environment monitoring, etc. However, to the best of our knowledge, there is no top-down approach to online 3D multi-view MOT that is capable of producing comparable results with the aforementioned data-centric batch-processing approaches.

At the other end of the spectrum are the model-centric approaches that rely largely on physical models of the dynamics of the objects, the geometry and characteristics of the sensors/cameras. From a state-space modeling perspective, a natural choice for online MOT is the multi-object Bayes filter [28]. Since the inception of the Random Finite Sets (RFS) framework for multi-object state-space models, a number of multi-objects Bayesian filters have been developed [29], [30] and applied to visual MOT problems [2], [4], [31]. The latest is the Generalized labeled Multi-Bernoulli (GLMB) filter, an analytic solution to the multi-object Bayes filter that jointly estimates the number of objects and their trajectories online [32]. The salient feature of this approach is that it seamlessly integrates track management, state estimation, clutter rejection, occlusion/mis-detection handling and multiple sensor data into a single recursion [4]. In this article, we

TABLE 1
Basic Notation

Symbol	Description
a^T	Transpose of vector/matrix a
\otimes	Kronecker product on two matrices
I_n	Identity matrix of n dimension
$0_{n \times m}$	Zero matrix of n by m dimension
$\text{diag}(\cdot)$	Converts any vector to a diagonal matrix
$X_{m:n}$	X_m, X_{m+1}, \dots, X_n
$\langle f, g \rangle$	$\int f(x)g(x)dx$
h^X	$\prod_{x \in X} h(x)$ where $h^0 = 1$
$\delta_Y[X]$	Kronecker delta function, 1 if $X = Y$, 0 otherwise
$1_Y(x)$	Indicator function, 1 if $x \in Y$, 0 otherwise
$\mathcal{N}(\cdot; \mu, P)$	Gaussian pdf with mean μ and covariance P

demonstrate how this framework can be used to develop a competitive online 3D multi-view MOT solution.

In addition to algorithms, datasets for performance evaluation is an important aspect of 3D multi-view MOT research. Existing multi-view datasets include DukeMTMC [33], PETS 2009 S2.L1 [34], EPFL - Laboratory, Terrace and Passageway [14], SALSA [35], Campus [8] and EPFL-RLC [15]. We refer the reader to [16], Section 2.1, for a descriptive comparison among the aforementioned datasets. However, these datasets are either poor in resolution [33], [34], non-overlapping in views [33], or not sufficiently crowded [7], [8], [14], and thus not adequate for more rigorous performance evaluations. Recently, in [16], a seven-camera high-definition (HD) unscripted pedestrian dataset known as WILDTRACKS was introduced to provide a high quality, highly crowded and cluttered evaluation scenario. It comes with accurate joint (extrinsic and intrinsic) calibration, and 7 series of 400 annotated frames for detection at a rate of 2 frames per second (fps). The annotations of the tracks are given both as locations on the ground plane and 2D bounding boxes projected onto each view.

While WILDTRACKS is more extensive than earlier datasets, it is still not sufficient for comprehensive 3D MOT performance evaluation. Specifically, it does not provide the camera locations/parameters needed for testing and evaluation of model-centric solutions that exploit multi-camera geometry. For actual 3D MOT applications where objects may also move vertically (e.g. sport analytics, age care, etc.), ground plane annotations are simply not adequate for evaluating tracking performance. Moreover, WILDTRACKS does not have scenarios for testing occlusion handling (and hence tracking) in highly populated tight spaces. To enrich the datasets and addressing the aforementioned concerns, we propose the Curtin Multi-Camera (CMC) dataset that comprises four calibrated cameras, on scenarios of varying difficulties in crowd density and occlusion, as well as scenarios with people jumping and falling, all with 3D centroid annotations, along with camera locations and parameters.

3 BAYESIAN FORMULATION

This section formulates the multi-view MOT problem, including our new detection model, and its occlusion handling capability via optimal Bayesian estimation. The notations used in this paper are tabulated in Table 1.

3.1 Object Dynamics

An existing object at time k is represented by a state $\mathbf{x} = (x, \ell)$, where x is a vector of features in some space \mathbb{X} , while

ℓ is a unique label consisting of the object's time of birth and an index to distinguish those born at the same time [32]. An object either survives with probability $P_S(\mathbf{x})$ and evolves to state $\mathbf{x}_+ = (x_+, \ell_+)$ at the next time with transition density

$$f_{S,+}(\mathbf{x}_+|\mathbf{x}) = f_{S,+}(x_+|x, \ell)\delta_\ell[\ell_+], \quad (1)$$

or dies with probability $1 - P_S(\mathbf{x})$. At this next time, an object with label ℓ is born with probability $P_{B,+}^{(\ell)} \triangleq P_{B,+}(\ell)$, and with feature-vector x distributed according to a probability density $f_{B,+}^{(\ell)}(\cdot) \triangleq f_{B,+}(\cdot, \ell)$. Note that the label of an object remains the same over time, and hence the *trajectory* of an object is a sequence of consecutive states with a common label [32].

Denote by \mathbb{B}_k is the (finite) set of all possible labels for objects born at time k , then the label space for all objects up to time k is the disjoint union $\mathbb{L}_k = \bigsqcup_{t=0}^k \mathbb{B}_t$, and hence the state space is $\mathbb{X} \times \mathbb{L}_k$. Let $\mathcal{L}(\mathbf{x})$ denotes the label of an $\mathbf{x} \in \mathbb{X} \times \mathbb{L}_k$. For any finite $\mathbf{X} \subset \mathbb{X} \times \mathbb{L}_k$, we define $\mathcal{L}(\mathbf{X}) \triangleq \{\mathcal{L}(\mathbf{x}) : \mathbf{x} \in \mathbf{X}\}$, and the *distinct label indicator* $\Delta(\mathbf{X}) \triangleq \delta_{|\mathbf{X}|}(|\mathcal{L}(\mathbf{X})|)$. At any time, the set \mathbf{X} of (states of) objects in the scene must have distinct labels, i.e. $\Delta(\mathbf{X}) = 1$. Conditional on the current set of objects, it is standard practice to assume that objects are born or displaced at the next time, independently of one another. For simplicity we omit the subscript k .

3.2 Multi-Sensor Observations

Suppose that at time k , there are C cameras (sensors), and a set \mathbf{X} of current objects. Each $\mathbf{x} \in \mathbf{X}$ is either: detected by camera $c \in \{1:C\}$, with probability $P_D^{(c)}(\mathbf{x}; \mathbf{X})$ and generates an observation $z^{(c)}$ in the measurement space $\mathbb{Z}^{(c)}$ with likelihood $g^{(c)}(z^{(c)}|\mathbf{x})$; or missed with probability $1 - P_D^{(c)}(\mathbf{x}; \mathbf{X})$. Note that to account for occlusions (and uncertainty in the detection process), the probability of detecting an object also depends on the states of other current objects. However, most MOT algorithms neglects the dependence on \mathbf{X} for computational tractability. The detection process also generates false positives at camera c , usually characterised by an intensity function $\kappa^{(c)}$ on $\mathbb{Z}^{(c)}$. Specifically, the number of false positives is Poisson distributed with mean $\langle \kappa^{(c)}, 1 \rangle$, and the false positives themselves are i.i.d. according to the probability density $\kappa^{(c)}/\langle \kappa^{(c)}, 1 \rangle$. It is standard to assume that, conditional on the set \mathbf{X} of objects, detections are independent from false positives, and that the set $Z^{(c)}$ of detections and false positives at sensor c , are independent from those at other sensors.

A hypothesis associating observations, at time k , from camera c to labels is represented by a positive 1-1 map¹ $\gamma^{(c)}$, with domain \mathbb{L}_k and range $\{-1:|Z^{(c)}|\}$, as follows: $\gamma^{(c)}(\ell) = -1$ means object ℓ does not exist; $\gamma^{(c)}(\ell) = 0$ means object ℓ is not detected by camera c ; $\gamma^{(c)}(\ell) > 0$ means object ℓ generates detection $z_{\gamma^{(c)}(\ell)}$ at camera c . We call

$$\mathcal{L}(\gamma^{(c)}) \triangleq \{\ell \in \mathbb{L}_k : \gamma^{(c)}(\ell) \geq 0\}, \quad (2)$$

the *live labels* of $\gamma^{(c)}$, and $\Gamma^{(c)}$ the set of all positive 1-1 maps with domain \mathbb{L}_k and range $\{-1:|Z^{(c)}|\}$. Moreover,

1. A map is positive 1-1 if no two distinct arguments are mapped to the same positive value [32]. This property ensures that each detection comes from at most one object.

$\gamma \triangleq (\gamma^{(1:C)})$ is said to be positive 1-1 if all constituent $\gamma^{(1)}, \dots, \gamma^{(C)}$ are positive 1-1 and have the same live labels. Similarly, we denote $\mathcal{L}(\gamma)$ as the *live labels* of γ (which is the same as the live labels of any of its constituent component), and Γ as the set of all positive 1-1 γ .

Under standard assumptions, the likelihood that \mathbf{X} generates $Z^{(c)}$ at camera c is given by the following sum over the space $\Gamma^{(c)}$ of positive 1-1 maps with domain \mathbb{L}_k and range $\{-1:|Z^{(c)}|\}$ [32]:

$$g^{(c)}(Z^{(c)}|\mathbf{X}) \propto \sum_{\gamma^{(c)} \in \Gamma^{(c)}} \delta_{\mathcal{L}(\gamma^{(c)})}[\mathcal{L}(\mathbf{X})] \left[\psi_{Z^{(c)}, \mathbf{X}}^{(c, \gamma^{(c)} \circ \mathcal{L}(\cdot))}(\cdot) \right]^{\mathbf{X}}, \quad (3)$$

where $\gamma^{(c)} \circ \mathcal{L}(\mathbf{x}) = \gamma^{(c)}(\mathcal{L}(\mathbf{x}))$, and

$$\psi_{\{z_{1:M}\}, \mathbf{X}}^{(c, j)}(\mathbf{x}) = \begin{cases} \frac{P_D^{(c)}(\mathbf{x}; \mathbf{X}) g^{(c)}(z_j | \mathbf{x})}{\kappa^{(c)}(z_j)}, & j = 1:M \\ 1 - P_D^{(c)}(\mathbf{x}; \mathbf{X}), & j = 0 \end{cases}. \quad (4)$$

Note that since $Z^{(c)}$ is a set, the likelihood is constructed via Mahler's set density [29], [30], which can be treated like a probability density [36]. The likelihood that \mathbf{X} generates the multi-sensor observation $Z \triangleq (Z^{(1:C)})$ is the product $\prod_{c=1}^C g^{(c)}(Z^{(c)}|\mathbf{X})$, which can be written as [19]

$$g(Z|\mathbf{X}) \propto \sum_{\gamma \in \Gamma} \delta_{\mathcal{L}(\gamma)}[\mathcal{L}(\mathbf{X})] \left[\psi_{Z, \mathbf{X}}^{(\gamma \circ \mathcal{L}(\cdot))}(\cdot) \right]^{\mathbf{X}}, \quad (5)$$

where

$$\delta_{\mathcal{L}(\gamma)}[J] \triangleq \prod_{c=1}^C \delta_{\mathcal{L}(\gamma^{(c)})}[J], \quad (6)$$

$$\psi_{Z, \mathbf{X}}^{(j^{(1:C)})}(\mathbf{x}) \triangleq \prod_{c=1}^C \psi_{Z^{(c)}, \mathbf{X}}^{(c, j^{(c)})}(\mathbf{x}). \quad (7)$$

Remark: The sets of objects, observations, and possibly the number of sensors and their parameters, may vary with time. However, for clarity we suppressed the time index.

3.3 Bayes Filter

Under the Bayesian paradigm, all information on the set of objects is captured in the (multi-object) posterior, which can be recursively computed, albeit with very high computational cost. A more tractable alternative is the (multi-object) filtering density², which captures all information on the current set of objects. The multi-object posterior/filtering density intrinsically encapsulates complementary information captured in the multi-view multi-object likelihood function (with a suitable detection model), thereby enables optimal inference of the trajectories in the presence of occlusions.

The multi-object filtering density can be propagated forward by the (multi-object) Bayes recursion [29], [30]

$$\pi_+(\mathbf{X}_+) \propto g(Z_+|\mathbf{X}_+) \int \mathbf{f}_+(\mathbf{X}_+|\mathbf{X}) \pi(\mathbf{X}) \delta \mathbf{X}, \quad (8)$$

where: π and π_+ denote the multi-object filtering densities³ at times k and $k+1$, respectively; the integral is the set integral [30]; and \mathbf{f}_+ is the multi-object transition kernel (whose actual expression not needed in this work, but can be found in e.g. [32]). Under the standard dynamic and observation

2. We use Mahler's set density/integral for random finite sets [29].

3. The filtering densities are conditioned on the observations, which have been omitted for notational compactness.

models described in the previous subsections, and with $P_D^{(c)}(\mathbf{x}; \mathbf{X}) = P_D^{(c)}(\mathbf{x})$, the filtering recursion (8) admits an analytical solution known as Generalized Labeled Multi-Bernoulli (GLMB) filter [32]. This filter can be efficiently implemented for online MOT [37], by exploiting conjugacy of GLMBs with respect to the multi-object likelihood. In practice $P_D^{(c)}(\mathbf{x})$ is usually independent of \mathbf{x} .

A detection probability (of an object \mathbf{x}) that does not depend on other objects, i.e. $\mathbf{X} - \{\mathbf{x}\}$, is unable to capture the effect of occlusions. On the other hand, accounting for occlusions with $P_D^{(c)}(\mathbf{x}; \mathbf{X})$ that actually depends on \mathbf{X} , results in filtering densities that are not GLMBs. One example is the merged-measurement model [38], which involves summing over all partitions of the set \mathbf{X} , making it intractable [38]. While the resulting filtering density can be approximated by a GLMB with matching cardinality distribution and first moment, this solution is still computationally demanding, not suitable for large number of objects. In what follows, we propose a new detection model that addresses occlusions and permits efficient multi-view MOT implementations.

3.4 Detection Model

For tracking in 3D, we consider the feature-vector $\mathbf{x} = (x^{(p)}, \dot{x}^{(p)}, x^{(s)})$, where: $x^{(p)}$ is the object's position (centroid) in 3D Cartesian coordinates; $\dot{x}^{(p)}$ is its velocity; and $x^{(s)}$ is its shape parameter. The region in \mathbb{R}^3 occupied by an object with labeled state $\mathbf{x} = (x, \ell)$ is denoted by $R(\mathbf{x})$.

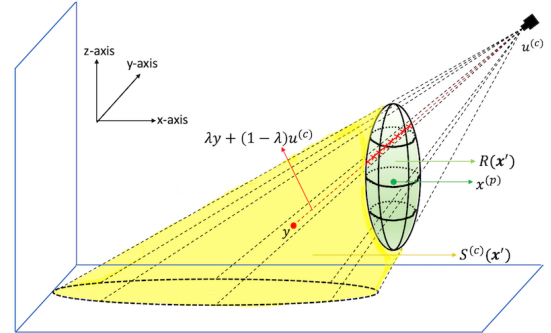


Fig. 1. The shadow region (in yellow) of object with labeled state \mathbf{x}' , relative to camera c .

Consider camera c and the set \mathbf{X} of current objects. In this work, an object $(x, \ell) \in \mathbf{X}$ is regarded as occluded from camera c when its position $x^{(p)}$ is not in the line of sight (LoS) of the camera, i.e. $x^{(p)}$ is in the shadow regions of the other objects in \mathbf{X} . Assuming a straight LoS, the shadow region of an object with labeled state \mathbf{x}' , relative to camera c (see Fig. 1), is given by

$$S^{(c)}(\mathbf{x}') = \left\{ y \in \mathbb{R}^3 : \overline{(u^{(c)}, y)} \cap R(\mathbf{x}') \neq \emptyset \right\}, \quad (9)$$

where $\overline{(u^{(c)}, y)} \triangleq \{ \lambda y + (1 - \lambda) u^{(c)} : \lambda \in [0, 1] \}$ is the line segment joining the position $u^{(c)}$ of camera c and y . Note that for an ellipsoidal region $R(\mathbf{x}')$, the indicator function $1_{S^{(c)}(\mathbf{x}')}(y)$ of its shadow region can be computed in closed form (see Section 4.1).

To incorporate the effect of occlusions into the detection model, the probability that $\mathbf{x} \in \mathbf{X}$ be detected by camera c should diminish to a small value when it is occluded from camera c , i.e. when its position $x^{(p)} \in \bigcup_{\mathbf{x}' \in \mathbf{X} - \mathbf{x}} S^{(c)}(\mathbf{x}')$.

This can be accomplished by extending the standard detection probability $P_D^{(c)}(\mathbf{x})$, to

$$P_D^{(c)}(\mathbf{x}; \mathbf{X}) = P_D^{(c)}(\mathbf{x})\Omega^{(c)}(\mathcal{L}(\mathbf{x}); \mathbf{X}), \quad (10)$$

where

$$\Omega^{(c)}(\ell; \{(x, \ell), \mathbf{x}_1, \dots, \mathbf{x}_n\}) = 1 - \beta 1_{\bigcup_{i=1}^n S^{(c)}(\mathbf{x}_i)}(x^{(p)}), \quad (11)$$

$\beta \in [0, 1]$ (usually chosen to be close to 1). Note that, when \mathbf{x} is in the LoS of camera c , the detection probability is $P_D^{(c)}(\mathbf{x})$, and when it is occluded by the other objects the detection probability scales down to $P_D^{(c)}(\mathbf{x})(1 - \beta)$.

Conditional on detection, \mathbf{x} is observed at camera c as a bounding box $z^{(c)} \triangleq (z_p^{(c)}, z_e^{(c)})$, where $z_p^{(c)}$ is the center, and $z_e^{(c)}$ is the extent, parameterized by the logarithms of the width (x-axis) and height (y-axis), in image coordinates. This observation process can be modeled by the likelihood:

$$g^{(c)}(z^{(c)}|\mathbf{x}) = \mathcal{N}\left(z^{(c)}; \Phi^{(c)}(\mathbf{x}) + \begin{bmatrix} 0_{2 \times 1} \\ -v_e^{(c)}/2 \end{bmatrix}, \text{diag}\left(\begin{bmatrix} v_p^{(c)} \\ v_e^{(c)} \end{bmatrix}\right)\right), \quad (12)$$

where: $\Phi^{(c)}(\mathbf{x})$ is the box bounding the image of $R(\mathbf{x})$ in the camera's image plane, under the camera projection; $v_p^{(c)}$ and $v_e^{(c)}$ are respectively the vector of noise variances for the center and the extent (in logarithm) of the box. This Gaussian model of the logarithms of the width and height is equivalent to modeling the actual width and height as log-normals, which ensures that they are non-negative. Note that these log-normals have mean 1, and variances $e^{v_{e,1}^{(c)}} - 1$ and $e^{v_{e,2}^{(c)}} - 1$, where $v_{e,1}^{(c)}$ and $v_{e,2}^{(c)}$ are the two components of $v_e^{(c)}$. This means the observed width and height are randomly scaled versions of their nominal values, with an expected scaling factor of 1.

The camera projection is determined by the camera matrix $P_{3 \times 4}^{(c)}$, which projects homogeneous points in world coordinate frame to homogeneous points in the image plane of camera c , and can be obtained by standard calibration techniques (see [39] for details). Note that for an ellipsoidal region $R(\mathbf{x})$, the axis-aligned bounding box $\Phi^{(c)}(\mathbf{x})$ on the image plane can be computed analytically (see Section 4.1).

3.5 Multi-view GLMB Update with Occlusions

This subsection presents a tractable approximation to the multi-view Bayes update for the above detection model, to address occlusions. Specifically, we adopt a GLMB approximation that admits efficient online implementation.

Suppose that the multi-object prior is a GLMB [32] of the form

$$\pi(\mathbf{X}) = \Delta(\mathbf{X}) \sum_{\xi} w^{(\xi)}(\mathcal{L}(\mathbf{X})) [p^{(\xi)}]^{\mathbf{X}}, \quad (13)$$

where ξ is an index ranging over a discrete space Ξ , each $p^{(\xi)}(\cdot, \ell)$ is a probability density on \mathbb{X} , and each $w^{(\xi)}(J)$ is non-negative with $\sum_{J \in \Xi} w^{(\xi)}(J) = 1$. Then, using Bayes rule with the likelihood (7) yields the updated multi-object density

$$\pi_Z(\mathbf{X}) \propto \Delta(\mathbf{X}) \sum_{\xi, \gamma} \delta_{\mathcal{L}(\gamma)}[\mathcal{L}(\mathbf{X})] w^{(\xi)}(\mathcal{L}(\mathbf{X})) [p_{Z, \mathbf{X}}^{(\xi, \gamma)}]^{\mathbf{X}}, \quad (14)$$

where

$$p_{Z, \mathbf{X}}^{(\xi, \gamma)}(\mathbf{x}) = \psi_{Z, \mathbf{X}}^{(\gamma \circ \mathcal{L}(\mathbf{x}))}(\mathbf{x}) p^{(\xi)}(\mathbf{x}). \quad (15)$$

As previously alluded to, the updated multi-object density (14) is not a GLMB because $p_{Z, \mathbf{X}}^{(\xi, \gamma)}$ also depends on \mathbf{X} .

Note from the definition of $\psi_{Z, \mathbf{X}}^{(\gamma \circ \mathcal{L}(\mathbf{x}))}(\mathbf{x})$, i.e. (4), (7), and the detection model (10) that $\Omega^{(c)}(\ell; \mathbf{X})$ is the only constituent term of $p_{Z, \mathbf{X}}^{(\xi, \gamma)}(\mathbf{x})$ that depends on \mathbf{X} , the rest are functions of \mathbf{x} only. Additionally, $\Omega^{(c)}$ only take on two values, 1 and $1 - \beta$. Thus, a good approximation of $\Omega^{(c)}(\ell; \mathbf{X})$, and hence $p_{Z, \mathbf{X}}^{(\xi, \gamma)}$, can be obtained by replacing \mathbf{X} by its $p^{(\xi)}$ -predicted value $\mathbf{X}^{(\xi, \mathcal{L}(\gamma))} = \{(x^{(\xi, \ell)}, \ell) : \ell \in \mathcal{L}(\gamma)\}$, where $x^{(\xi, \ell)}$ denotes an estimate (e.g. mean, mode) from the prior/prediction (probability) density $p^{(\xi)}(\cdot, \ell)$. Moreover, approximating $p_{Z, \mathbf{X}}^{(\xi, \gamma)}$ by $p_{Z, \mathbf{X}^{(\xi, \mathcal{L}(\gamma))}}^{(\xi, \gamma)}$ turns (14) into a GLMB since $p_{Z, \mathbf{X}^{(\xi, \mathcal{L}(\gamma))}}^{(\xi, \gamma)}$ does not depend on \mathbf{X} . Hence, in this work, we propose to approximate the Bayes updated multi-object density (14) by the GLMB

$$\hat{\pi}_Z(\mathbf{X}) \propto \Delta(\mathbf{X}) \sum_{\xi, \gamma} \delta_{\mathcal{L}(\gamma)}[\mathcal{L}(\mathbf{X})] w^{(\xi)}(\mathcal{L}(\mathbf{X})) [p_{Z, \mathbf{X}^{(\xi, \mathcal{L}(\gamma))}}^{(\xi, \gamma)}]^{\mathbf{X}} \quad (16)$$

3.6 Multi-view GLMB Filtering with Occlusions

Starting with a GLMB filtering density π , the prediction integral in (8) is also a GLMB [32] and hence, the approximate update of the previous subsection applies. Consequently, the approximate multi-view GLMB filtering density can be propagated via the standard (multi-sensor) GLMB filter [19] by adapting the detection model (in accordance with the predicted multi-object state), at each time, so that the detection probability is scaled by $(1 - \beta)$ when a predicted object is not in the LoS. The prediction and (approximate) update can be combined into a single recursion as follows.

Suppose that the current the multi-object GLMB filtering density has the form (13), then the GLMB filtering density at the next time is given by [19]

$$\pi_+(\mathbf{X}_+) \propto \Delta(\mathbf{X}_+) \sum_{\xi, \gamma_+, I} 1_{\mathcal{F}(\mathbb{B}_+ \uplus I)}(\mathcal{L}(\gamma_+)) \delta_{\mathcal{L}(\gamma_+)}[\mathcal{L}(\mathbf{X}_+)] \times \left[\omega_{\mathbf{X}_+^{(\xi, \mathcal{L}(\gamma_+))}}^{(\xi, \gamma_+)} \right]^{\mathbb{B}_+ \uplus I} w^{(\xi)}(I) \left[p_{Z_+, \mathbf{X}_+^{(\xi, \mathcal{L}(\gamma_+))}}^{(\xi, \gamma_+)} \right]^{\mathbf{X}_+}, \quad (17)$$

where $\gamma_+ \in \Gamma_+$, $I \subset \mathbb{L}$, $\mathcal{F}(\mathbb{B}_+ \uplus I)$ represents all (finite) subsets of $\mathbb{B}_+ \uplus I$, $\mathcal{L}(\gamma_+)$ is the set of live labels of γ_+ and,

$$\omega_{\mathbf{Y}}^{(\xi, \gamma_+)}(\ell) = \begin{cases} 1 - \bar{P}_S^{(\xi)}(\ell), & \ell \in \overline{\mathcal{L}(\gamma_+)} - \mathbb{B}_+ \\ \bar{\Lambda}_{S, \mathbf{Y}}^{(\xi, \gamma_+)}(\ell), & \ell \in \mathcal{L}(\gamma_+) - \mathbb{B}_+ \\ 1 - P_{B, +}(\ell), & \ell \in \mathcal{L}(\gamma_+) \cap \mathbb{B}_+ \\ \bar{\Lambda}_{B, \mathbf{Y}}^{(\gamma_+)}(\ell), & \ell \in \mathcal{L}(\gamma_+) \cap \mathbb{B}_+ \end{cases}, \quad (18)$$

$$p_{Z_+, \mathbf{Y}}^{(\xi, \gamma_+)}(x_+, \ell) \propto \begin{cases} \langle \Lambda_{S, \mathbf{Y}}^{(\gamma_+)}(x_+ | \cdot, \ell), p^{(\xi)}(\cdot, \ell) \rangle, & \ell \in \mathcal{L}(\gamma_+) - \mathbb{B}_+ \\ \Lambda_{B, \mathbf{Y}}^{(\gamma_+)}(x_+, \ell), & \ell \in \mathcal{L}(\gamma_+) \cap \mathbb{B}_+ \end{cases} \quad (19)$$

$$\bar{P}_S^{(\xi)}(\ell) = \langle P_S(\cdot, \ell), p^{(\xi)}(\cdot, \ell) \rangle, \quad (20)$$

$$\Lambda_{B, \mathbf{Y}}^{(\gamma_+)}(x_+, \ell) = \psi_{Z_+, \mathbf{Y}}^{(\gamma_+)}(x_+, \ell) f_{B, +}(x_+, \ell) P_{B, +}(\ell), \quad (21)$$

$$\Lambda_{S, \mathbf{Y}}^{(\gamma_+)}(x_+ | y, \ell) = \psi_{Z_+, \mathbf{Y}}^{(\gamma_+)}(x_+, \ell) f_{S, +}(x_+ | y, \ell) P_S(y, \ell), \quad (22)$$

$$\bar{\Lambda}_{B, \mathbf{Y}}^{(\gamma_+)}(\ell) = \int \Lambda_{B, \mathbf{Y}}^{(\gamma_+)}(x, \ell) dx, \quad (23)$$

$$\bar{\Lambda}_{S,Y}^{(\xi,\gamma+(\ell))}(\ell) = \int \langle \Lambda_{S,Y}^{(\gamma+(\ell))}(x|\cdot, \ell), p^{(\xi)}(\cdot, \ell) \rangle dx, \quad (24)$$

$$\mathbf{X}_+^{(\xi,J)} = \{(\mathbf{x}_+^{(\xi,\ell)}, \ell) : \ell \in J\}. \quad (25)$$

and $\mathbf{x}_+^{(\xi,\ell)}$ denotes an estimate (e.g. mean, mode) from the prediction density i.e., birth density $f_{B,+}(\mathbf{x}_+, \ell)$ if $\ell \in \mathbb{B}_+$ or $\int f_{S,+}(\mathbf{x}_+|y, \ell) p^{(\xi)}(y, \ell) dy$ if $\ell \in I$.

Remark: If the initial prior is a GLMB, and the measurements are point detections, then ξ is indeed the history of the (multi-sensor) association maps up to k , i.e., $\xi \triangleq \gamma_{1:k}$.

Given the GLMB (13), the multi-object state estimate can be obtained by first determining: the most probable cardinality n^* from the cardinality distribution [19]

$$\text{Prob}(|\mathbf{X}| = n) = \sum_{J,\xi} \delta_n[|J|] w^{(\xi)}(J); \quad (26)$$

and then the component (J^*, ξ^*) with highest weight such that $|J^*| = n^*$. The state estimate for each object $\ell \in J^*$ can be computed from $p^{(\xi^*)}(\cdot, \ell)$, e.g. the mode or mean.

Remark: An alternative is the multi-object *trajectory* estimator that uses the joint density of states along the object's *trajectory* (over time) [19]. This joint density is computable because for each ℓ we can trace the initial state distribution in the LMB birth model, and the entire *trajectory* from ξ^* . Moreover, its marginals can be computed recursively from $p^{(\xi^*)}(\cdot, \ell)$ using the forward-backward algorithm [19], [40].

4 IMPLEMENTATION

Having described how GLMB filtering can be applied to resolve occlusions in multi-view settings with a suitable detection model, we now describe how the filter is implemented for people tracking in 3D.

4.1 Object Representation and Model Parameters

Each object is represented by an axis-aligned ellipsoid. For an object with labeled state $\mathbf{x} = (x, \ell)$, the position $x^{(p)}$ is the centroid, and the shape parameter $x^{(s)}$ is a vector containing the logarithms of the half-lengths of the ellipsoid's principle axes. Further, the time-evolution of the state vector \mathbf{x} is modelled by a linear Gaussian transition density:

$$f_{S,+}(\mathbf{x}_+|\mathbf{x}, \ell) = \mathcal{N}\left(\mathbf{x}_+; \mathbf{F}\mathbf{x} + \begin{bmatrix} 0_{6 \times 1} \\ -v^{(s)}/2 \end{bmatrix}, \mathbf{Q}\right), \quad (27)$$

where

$$\mathbf{F} = \begin{bmatrix} \mathbf{I}_3 \otimes \begin{bmatrix} 1 & T \\ 0 & 1 \end{bmatrix} & 0_{6 \times 3} \\ \hline 0_{3 \times 6} & \mathbf{I}_3 \end{bmatrix}, \quad (28)$$

$$\mathbf{Q} = \begin{bmatrix} \text{diag}(v^{(p)}) \otimes \begin{bmatrix} T^2 \\ T \end{bmatrix} & \begin{bmatrix} T^2 & T \end{bmatrix} & 0_{6 \times 3} \\ \hline 0_{3 \times 6} & \text{diag}(v^{(s)}) \end{bmatrix}, \quad (29)$$

T is the sampling period, $v^{(p)}$ and $v^{(s)}$ are, respectively, 3D vectors of noise variances for the components of the centroid and shape parameter (in logarithm) of the ellipsoid. This transition density describes a nearly constant velocity model for the centroid and a Gaussian random-walk for the shape parameter. Gaussianity of the logarithms of the half-lengths is equivalent to modeling the half-lengths as log-normals, which ensure that they are non-negative. Note

that these log-normals have mean 1, and variances $e^{v_i^{(s)}} - 1$, $i = 1, 2, 3$, where $v_i^{(s)}$ is the i^{th} components of $v^{(s)}$. Hence, the observed half-lengths are randomly scaled versions of their nominal values, with an expected scaling factor of 1.

Empirically, objects in the scene for a long time are more likely to remain in the scene unless they are close to the borders (exit regions). This can be modelled via the following object survival probability [4]:

$$P_S(\mathbf{x}, \ell) = \frac{b(\mathbf{x})}{1 + \exp(-\tau(k - \ell[1, 0]^T))}, \quad (30)$$

where $b(\mathbf{x})$ is the scene mask (chosen to be close to one in the middle of the scene, and close to zero in the designated exit regions), and τ is the control parameter for the age-dependent survival probability.

For ellipsoids, the shadow region indicator (11) of the detection model proposed in Subsection 3.4, has a close form. To determine whether a line intersects an ellipsoid amounts to determining whether the roots of a certain quadratic equation are real [41]. Consequently, for an axis-aligned ellipsoidal object representation, the shadow region indicator (11) of an object with labeled state \mathbf{y} is given by

$$1_{S^{(c)}(\mathbf{y})}(\mathbf{x}) = \begin{cases} 1, & (\mathcal{B}_{\mathbf{x}, \mathbf{y}}^{(c)})^2 - 4\mathcal{A}_{\mathbf{x}, \mathbf{y}}^{(c)}\mathcal{C}_{\mathbf{y}}^{(c)} \geq 0 \\ 0, & \text{otherwise} \end{cases}, \quad (31)$$

where

$$\mathcal{A}_{\mathbf{x}, \mathbf{y}}^{(c)} = (\mathbf{x}^{(p)} - \mathbf{u}^{(c)})^T \left(\text{diag}(\mathbf{y}^{(s)}) \right)^{-2} (\mathbf{x}^{(p)} - \mathbf{u}^{(c)}), \quad (32)$$

$$\mathcal{B}_{\mathbf{x}, \mathbf{y}}^{(c)} = (\mathbf{x}^{(p)} - \mathbf{u}^{(c)})^T \left[2 \left(\text{diag}(\mathbf{y}^{(s)}) \right)^{-2} \mathbf{u}^{(c)} + \mathbf{d}_{\mathbf{y}} \right], \quad (33)$$

$$\mathcal{C}_{\mathbf{y}}^{(c)} = (\mathbf{u}^{(c)})^T \left[\left(\text{diag}(\mathbf{y}^{(s)}) \right)^{-2} \mathbf{u}^{(c)} + \mathbf{d}_{\mathbf{y}} \right] + \mathcal{E}_{\mathbf{y}}, \quad (34)$$

$$\mathbf{d}_{\mathbf{y}} = -2 \frac{\mathbf{y}^{(p)}}{(\mathbf{y}^{(s)} \cdot \mathbf{y}^{(s)})}, \quad \mathcal{E}_{\mathbf{y}} = \left\| \mathbf{y}^{(p)} / \mathbf{y}^{(s)} \right\|_2^2 - 1, \quad (35)$$

and $\mathbf{u}^{(c)}$ is the position of camera c , with multiplication/division of two vectors of the same dimension to be understood as point-wise multiplication/division.

In addition, using projection of quadrics [42, pp. 201], the bounding box $\Phi^{(c)}(\mathbf{x})$ in the measurement likelihood (12) has the following close form

$$\Phi^{(c)}(\mathbf{x}) \triangleq \mathcal{Z}(\mathcal{P}^{(c)}(\mathbf{x})), \quad (36)$$

where

$$\mathcal{P}^{(c)}(\mathbf{x}) = \left(\mathbf{P}_{3 \times 4}^{(c)} \left[\begin{array}{c|c} (\text{diag}(\mathbf{x}^{(s)}))^{-2} & \mathbf{d}_{\mathbf{x}}/2 \\ \hline \mathbf{d}_{\mathbf{x}}^T/2 & \mathcal{E}_{\mathbf{x}} \end{array} \right] (\mathbf{P}_{3 \times 4}^{(c)})^T \right)^{-1}, \quad (37)$$

$$\mathcal{Z} \left(\begin{bmatrix} \mathbf{A} & \mathbf{r} \\ \mathbf{r}^T & q \end{bmatrix} \right) = \begin{bmatrix} -\mathbf{Q}\mathbf{D}^{-1}\mathbf{Q}^T\mathbf{r} \\ 2\nu \left\| [1, 0] \mathbf{Q}\mathbf{D}^{-0.5} \right\|_2 \\ 2\nu \left\| [0, 1] \mathbf{Q}\mathbf{D}^{-0.5} \right\|_2 \end{bmatrix}, \quad (38)$$

$$\nu = (\mathbf{r}^T \mathbf{Q}\mathbf{D}^{-1} \mathbf{Q}^T \mathbf{r} - q)^{0.5}, \quad (39)$$

\mathbf{Q} is the matrix containing the eigenvectors of \mathbf{A} , and \mathbf{D} is the diagonal matrix of the eigenvalues of \mathbf{A} .

In this work, the object's birth density $f_{B,+}^{(\ell)}(\cdot)$, single-object transition (27) and likelihood (12) are all Gaussians. Standard Kalman prediction and Unscented Kalman update are used to evaluate (19), which results in Gaussian $p^{(\xi)}(\cdot, \ell)$.

4.2 Multi-view GLMB Filter Truncation

The number of components of the multi-view GLMB filtering recursion in (17) grows super-exponentially over time. To maintain tractability, truncating “insignificant” components has shown to minimize the L_1 approximation error [19]. This truncation strategy can be formulated as an NP-hard multi-dimensional assignment problem [19]. Nonetheless, it can be solved by exploiting certain structural properties, and suitable adaptation of 2D assignment solutions such as Murty’s or Auction, with at best cubic complexity in the product of measurements across all sensors [19]. Such complexity is still infeasible for systems with many sensors.

Following [19], the high computational cost can be alleviated by using Gibbs sampling to generate “significant” components from a suitable discrete distribution. Given \mathbb{B}_+ and (I, ξ) , where $I \subset \mathbb{L}$ is the previous surviving set of labels, we represent γ_+ as

$$\gamma_+ = \begin{bmatrix} \gamma_{+,1} \\ \gamma_{+,2} \\ \vdots \\ \gamma_{+,P} \end{bmatrix} = \begin{bmatrix} \gamma_{+,1}^{(1)} & \gamma_{+,1}^{(2)} & \cdots & \gamma_{+,1}^{(C)} \\ \gamma_{+,2}^{(1)} & \gamma_{+,2}^{(2)} & \cdots & \gamma_{+,2}^{(C)} \\ \vdots & \vdots & \ddots & \vdots \\ \gamma_{+,P}^{(1)} & \gamma_{+,P}^{(2)} & \cdots & \gamma_{+,P}^{(C)} \end{bmatrix}, \quad (40)$$

where $\gamma_{+,n} \triangleq \gamma_+(\ell_n)$, $\ell_n \in \{\ell_{1:P}\}$ is the enumeration over $\mathbb{B}_+ \uplus I$ and $P = |\mathbb{B}_+ \uplus I|$. This representation ensures $1_{\mathcal{F}(\mathbb{B}_+ \uplus I)}(\mathcal{L}(\gamma_+)) = 1$, in (17). The aim is to sample γ_+ from a discrete probability distribution of the form [19]:

$$\pi(\gamma_+) \propto 1_{\Gamma_+}(\gamma_+) \prod_{n=1}^P \vartheta_n(\gamma_{+,n}), \quad (41)$$

where $\vartheta_n(\gamma_{+,n})$ is a distribution that is approximately proportional⁴ to $\omega_{\mathbf{x}_+^{(\xi, \mathcal{L}(\gamma_+))}}^{(\xi, \gamma_+)}(\ell_n)$ in (17), so that the samples are always positive 1-1, and those with high weights are more likely to be generated. Two Gibbs samplers based on two specific ϑ_n were considered in [19]. For scalability in the number of cameras, we adopt the computationally cheaper Minimally Markovian Gibbs sampler with linear complexity in the sum of total number of detections across all sensors, and quadratic complexity in the number of components [19].

The implementation of the multi-view GLMB recursion in (17) is the same as Algorithm 3 of [19] but with the additional computation of $\mathbf{X}_+^{(\xi, \mathcal{L}(\gamma_+))}$ according to (25). For tractability, integrations involving $P_D^{(c)}(\cdot)$ or $P_S(\cdot)$ with respect to $p^{(\xi)}(\cdot)$, are approximated by $P_D^{(c)}(\mathbf{x}^{(\xi, \ell)})$ or $P_S(\mathbf{x}^{(\xi, \ell)})$ respectively where $\mathbf{x}^{(\xi, \ell)} \in \mathbf{X}_+^{(\xi, \mathcal{L}(\gamma_+))}$. For completeness, the pseudocode is given in Algorithm 2 of Appendix 7.2.

5 EXPERIMENT

This section demonstrates two pertinent capabilities of our proposed methods. The first is the capability to produce 3D online estimates of object trajectories using independent monocular detections from different views. The second is the capability for uninterrupted or seamless operation in the event that cameras are added, removed or repositioned on

the fly. These experiments also test the performance of our detection model and 3D estimation under heavy occlusions.

We focus our demonstrations on the latest WILDTRACKS dataset, due to its relative advantages over existing datasets [16]. Performance comparisons are also undertaken with the state of the art methods presented in WILDTRACKS [16] which perform detection and tracking in the 2D ground plane. Since WILDTRACKS does not supply camera locations/parameters (which can be critical for 3D tracking solutions) our experiments rely on our best guess at the camera parameters, and performance comparisons are restricted to tracks in the 2D ground plane.

We further introduce a new four-camera 1920x1024 resolution Curtin Multi-Camera (CMC) dataset, that includes the camera matrices, camera locations and annotations for 3D centroid positions at 4fps. The new CMC dataset also includes scenarios with a high person density and significant visual occlusions across multiple cameras. We finally demonstrate the 3D tracking capability of our proposed method with the new CMC dataset.

The same object survival and detection model parameters are used for both datasets. Specifically: the survival probability $P_S(\mathbf{x})$ given by (30), is parameterized by the control parameter $\tau = 0.5$ and the scene mask $b(\cdot)$ with a margin of 0.3m inside the border of the tracking area; the detection probability $P_D^{(c)}(\mathbf{x}; \mathbf{X})$, given in Section 3.4 is parameterized by $P_D^{(c)}(\mathbf{x}) = \beta = 0.9$. For all cameras, the observed bounding box model is as described in (12), with position noise parameterized by $v_p^{(c)} = (400, 400)^T$, and the extent (in logarithm) noise by $v_e^{(c)} = (0.01, 0.0025)^T$.

5.1 Performance Evaluation Criteria

We evaluate the performance of the monocular detector and the 3D tracking results using the CLEAR MOT evaluation protocol along with the devkit provided in [43]. For detections, Multiple Object Detection Accuracy (MODA) is used to account for normalized false negatives (FN) and false positives (FP) and Multiple Object Detection Precision (MODP) is used to assess localization precision by spatial overlaps [44].

For 3D MOT, the following performance indicators are reported for a radius of 1m: Multiple Object Tracking Accuracy (MOTA) which penalizes FNs, FPs and identity switches (IDs) between consecutive frames; Multiple Object Tracking Precision (MOTP) which accounts for the overall dissimilarity between all true positives and the corresponding ground truth objects; Mostly Tracked (MT), Partially Tracked (PT), Mostly Lost (ML) which indicate how much of the trajectory is retained or lost by the tracker; Fragmentations (FM) which account for interrupted tracks based on ground truth trajectories; Identity Precision (IDP), Identity Recall (IDR) and F_1 score (IDF1) which are analogous to the standard precision, standard recall and F_1 score with identifications (tracks) [33]. Note that CLEAR MOT is traditionally calculated over the entire scenario window, and thus the tracking performance is reported after the entire data stream has been processed.

We also employ the OSPA⁽²⁾ metric [45], [46], [47] to evaluate the live or online tracking performance over time.

4. We say that two (unnormalized) distributions are approximately proportional when their normalized versions are approximately equal.

OSPA⁽²⁾ is based on the OSPA metric that captures both localization and cardinality errors between two finite sets. The OSPA⁽²⁾ metric is defined as the OSPA distance between two sets of tracks in some time window, and thus captures both localization and cardinality errors between the set of true and estimated tracks. This metric carries the interpretation of a time-averaged per-track error. It inherently penalizes switched tracks or label changes. In this study, the OSPA⁽²⁾ metric used is with order parameter 1, and cutoff parameter 1m, as well as a sliding window length $L_w = 10$ time frames.

5.2 WILDTRACKS Dataset

5.2.1 Model Parameters

The birth density is an adaptive LMB (see Section F in [48]) with $P_{B,+}^{(\ell)} = 0.001$ and $f_{B,+}^{(\ell)}(x) = \mathcal{N}(x; \mu_{B,+}^{(\ell)}, \Sigma_{B,+})$ where $\mu_{B,+}^{(\ell)}$ is obtained via clustering (e.g. k-means) and $\Sigma_{B,+} = 0.1^2 \mathbf{I}_9$. The single-object transition model is as described in (27) with position noise parameterized by $v^{(p)} = (0.0016, 0.0016, 0.0016)^T$, and the extent (in logarithm) noise by $v^{(s)} = (0.0036, 0.0036, 0.0004)^T$. Clutter follows a Poisson RFS with intensity $\kappa(z) = 10\mathcal{U}(\mathbb{Z})$ where $\mathcal{U}(\mathbb{Z})$ denotes a uniform density on the measurement region (giving a mean of 10 clutter points per frame).

5.2.2 Comparison with Deep-Occlusion+KSP+ptrack

It is imperative to note that Deep-Occlusion+KSP+ptrack performs preprocessing via a multiocular detector to produce measurements in the ground plane, followed by tracking with KSP, and motion post processing with ptrack in the ground plane [16]. On the other hand, the multi-view GLMB tracker takes independent monocular detections (via the YOLOv3 detector) from each camera as measurements, and then performs recursive filtering to resolve the multi-view data association and estimate 3D object trajectories. To compare the two methods, we project the 3D estimates from the former onto the ground plane.

Table 3 shows the CLEAR evaluation for various detectors, where the values for Deep-Occlusion are reproduced directly from [16]. We observe that monocular detections, in contrast to multiocular detections, are relatively poor due to severe occlusions in this dataset. Table 2 further shows the CLEAR MOT benchmark of the multi-view GLMB filter against the Deep-Occlusion+KSP+ptrack method (reproduced directly from [16]). While the latter exhibits lower IDs due to its inherent advantage in batch processing, there is a corresponding increase in FP and FN, which results in an overall penalty for the MOTA and MOTP scores. The multi-view GLMB filter exhibits a higher incidence of IDs due to its nature as a recursive filter as opposed to a batch algorithm. There is however a dramatic reduction in FP and FN, most likely due to improved tracking and data association, by making better use of the information available in the raw monocular detections. Overall, the multi-view GLMB filter exhibits an improvement in MOTA and MOTP scores, even though it only used a best guess of the unavailable camera parameters.

5.3 CMC Dataset and Multi-Camera Reconfiguration

5.3.1 New CMC Dataset

To the best of our knowledge, multi-view datasets such as WILDTRACKS are relatively rare, and are usually restricted to tracking in the ground plane. In order to validate the effectiveness of 3D tracking via the multi-view GLMB filter, as well as our proposed occlusion handling ability, the locations and parameters of the cameras must be available. To address this gap and demonstrate our proposed approach, we introduce a new CMC dataset recorded at 1920x1024 resolution with four calibrated cameras, each located at the top four corners of a room with dimensions 7.67m x 3.41m x 2.7m. Fig. 4 shows an overview of the tracking area. The CMC dataset features a number of different scenarios: CMC1 has a maximum of 3 people; CMC2 has a maximum of 10 people; CMC3 has a maximum of 15 people. Each person enters the tracking area at (2.03m, 0.71m) with an average height of 1.65m. The world coordinate frame is chosen such that the origin is at the lower left corner and the ground plane corresponds to the x-y plane at $z = 0$. Annotations are provided in the form of 3D centroid positions, along with camera locations and matrices for all scenarios and for all cameras respectively.

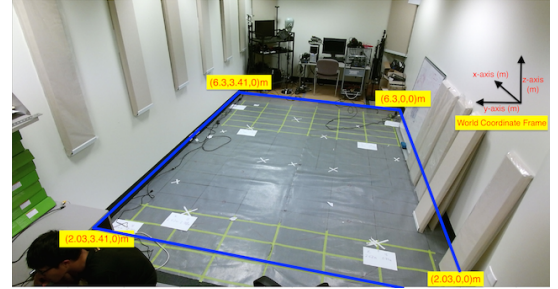


Fig. 4. Layout for CMC dataset: Blue lines denote the boundary of the tracking area. The yellow boxes denote the coordinates of the boundary in (x,y,z) axes. The 4 cameras are positioned (in sequence) at the top 4 corners of the room.

5.3.2 Multi-Camera Reconfiguration Setup

We design the experiment to demonstrate that our proposed algorithm does not require retraining, and maintains uninterrupted operation, in the event that cameras are added, removed or repositioned on the fly. Initially, two cameras are operating, which are then moved to different locations at a later time. Later in the scenario, two more cameras are added into the system one by one, one of which is randomly switched off and on over time. As there are no existing approaches that can track people in 3D, we benchmark this multi-camera reconfiguration experiment against an ideal case, wherein all cameras are always on.

It is important to note that there is a one-off pre-training on the monocular YOLOv3 detector for each camera. The two initially operational cameras are placed at positions 1 and 2 from times $k = 1$ to 50, and subsequently from times $k = 51$ to 100 the two cameras are placed at positions 3 and 4. This mimics the event that the cameras are moved to different locations. The sequence of camera reallocation, addition and deletion is shown in Fig. 5.

5.3.3 Model Parameters

The birth density is an LMB with parameters $P_{B,+}^{(\ell)} = 0.001$ and $f_{B,+}^{(\ell)}(x) = \mathcal{N}(x; \mu_{B,+}, \Sigma_{B,+})$ where $\mu_{B,+} =$

TABLE 2
CLEAR MOT benchmarks on WILDTRACKS dataset: \uparrow means higher is better while \downarrow means lower is better.

Tracker	IDF1 \uparrow	IDP \uparrow	IDR \uparrow	MT \uparrow	PT \downarrow	ML \downarrow	FP \downarrow	FN \downarrow	IDs \downarrow	FM \downarrow	MOTA \uparrow	MOTP \uparrow
Multi-view GLMB	76.9%	72.7%	81.7%	228	51	5	1226	377	219	36	74.6%	77.0%
Deep-Occlusion+KSP+ptrack	78.4%	84.4%	73.1%	72	74	25	2007	5830	103	95	72.2%	60.3%



Fig. 2. CMC2 Camera 1 to 4 (left to right): YOLOv3 detections (top row) and multi-view GLMB estimates (bottom row).

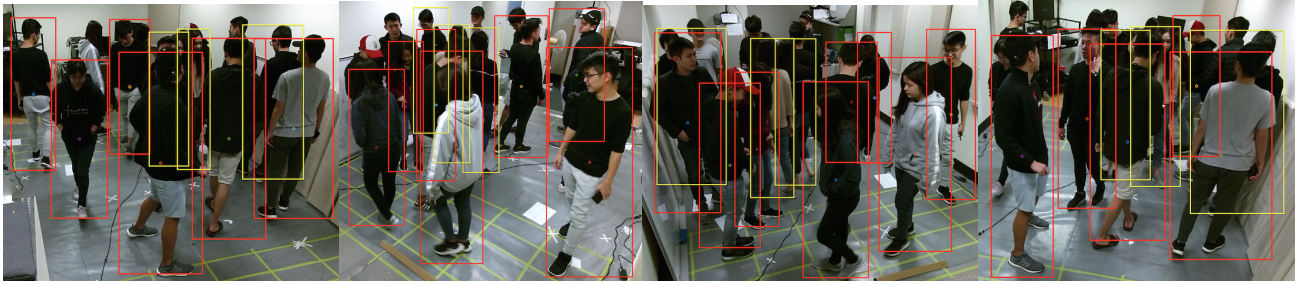


Fig. 3. CMC3 Camera 1 to 4 (left to right): YOLOv3 detections (red) and bounding boxes in yellow show people that are occluded in all four cameras.

TABLE 3
CLEAR evaluation for detection results on WILDTRACKS dataset.

Detector	MODA \uparrow	MODP \uparrow	Precision \uparrow	Recall \uparrow
YOLOv3-Cam1	12.2%	70.1%	0.55	0.62
YOLOv3-Cam2	31.7%	68.5%	0.68	0.58
YOLOv3-Cam3	-24.4%	69.2%	0.42	0.68
YOLOv3-Cam4	-272.4%	71.1%	0.14	0.57
YOLOv3-Cam5	-94.4%	70.0%	0.29	0.69
YOLOv3-Cam6	-12.6%	63.4%	0.44	0.50
YOLOv3-Cam7	-79.2%	70.1%	0.33	0.77
Deep-Occlusion	74.1%	53.8%	0.95	0.80

$[2.03 \ 0 \ 0.71 \ 0 \ 0.825 \ 0 \ -1.2 \ -1.2 \ -0.18]^T$ and $\Sigma_{B,+} = 0.1^2 I_9$. The single-object transition model is as described in (27) with position noise parameterized by $v^{(p)} = (0.0012, 0.0012, 0.0012)^T$, and the extent (in logarithm) noise by $v^{(s)} = (0.0036, 0.0036, 0.0004)^T$.

The same clutter model parameters are used in all scenarios of the CMC dataset. Specifically: the clutter follows a Poisson RFS with intensity $\kappa(z) = 3\mathcal{U}(\mathbb{Z})$ (giving a mean of 3 clutter points per frame).

5.3.4 CLEAR MOT Benchmarks

The CLEAR evaluation for the monocular detections on each dataset are given in Table 5. The values indicate that detections in a single-view are poor due to occlusions. The CLEAR MOT benchmarks for the output of the multi-view GLMB filter are given in Table 4. Entries without an asterisk correspond to the benchmark case where all four cameras are always on, and entries with an asterisk denote the results for the multi-camera reconfiguration experiment. The

comparisons indicate that the reconfiguration experiment generally produces similar performance to the four camera benchmark. It can also be seen that the tracking performance degrades as the number of people in the scene increases, since the visual occlusions become more frequent and more difficult to resolve.

5.3.5 OSPA⁽²⁾ Evaluation

We also benchmark the reconfiguration experiments against the ideal case via the OSPA⁽²⁾ metric, as shown in Fig. 5, which provides an online performance assessment of the tracking at each time step. For the sparse scenario CMC1, the results are virtually identical, due to high observability. For the medium scenario CMC2, there is a slight degradation in performance, as observability decreases due to camera reconfiguration. For the dense scenario CMC3, the difference is more pronounced. When all four cameras are turned on from $k = 100$ to 150, the performance of the benchmark and reconfiguration experiments are relatively close, whereas at other times there is a noticeable drop in performance due to unavailability of one or more cameras. Note also the spikes in the error curve at the beginning and the end of the scenario, which are due to track initiation and termination mismatches with the ground truths. Overall, these results confirm that our proposed framework can accommodate on the fly multi-camera reconfiguration without retraining.

5.3.6 Discussion

For the sparse scenario CMC1, the OSPA⁽²⁾ plot in Fig. 5 shows a low error for entire scenario, which is consistent

TABLE 4

CLEAR MOT benchmarks for multi-view GLMB filter tracking results on CMC1, 2 and 3: \uparrow means higher is better while \downarrow means lower is better, and the asterisk denotes the results from the multi-camera reconfiguration experiment.

Dataset	IDF1 \uparrow	IDP \uparrow	IDR \uparrow	MT \uparrow	PT \downarrow	ML \downarrow	FP \downarrow	FN \downarrow	IDs \downarrow	FM \downarrow	MOTA \uparrow	MOTP \uparrow
CMC1	100.0%	100.0%	100.0%	3	0	0	0	0	0	0	100.0%	100.0%
CMC2	99.4%	99.7%	99.0%	11	0	0	6	20	0	1	98.7%	88.5%
CMC3	82.5%	82.7%	82.3%	15	0	0	92	106	56	27	91.5%	80.0%
CMC1*	100.0%	100.0%	100.0%	3	0	0	0	0	0	0	100.0%	100.0%
CMC2*	99.3%	99.7%	98.0%	11	0	0	7	23	0	4	98.6%	88.5%
CMC3*	82.3%	83.3%	81.4%	14	1	0	68	135	38	26	91.0%	77.8%

TABLE 5

CLEAR evaluation for YOLOv3 detector results on CMC1, 2 and 3.

Dataset	MODA \uparrow	MODP \uparrow	Precision \uparrow	Recall \uparrow
CMC1 - Cam 1	60.0%	80.2%	0.72	0.97
CMC1 - Cam 2	20.5%	78.8%	0.56	0.97
CMC1 - Cam 3	13.2%	79.7%	0.53	0.97
CMC1 - Cam 4	2.1%	79.7%	0.51	0.96
CMC2 - Cam 1	51.2%	76.2%	0.77	0.72
CMC2 - Cam 2	45.3%	76.5%	0.72	0.72
CMC2 - Cam 3	43.4%	77.2%	0.71	0.72
CMC2 - Cam 4	47.3%	77.7%	0.74	0.71
CMC3 - Cam 1	44.9%	76.4%	0.79	0.60
CMC3 - Cam 2	39.8%	75.3%	0.73	0.62
CMC3 - Cam 3	36.1%	74.4%	0.72	0.58
CMC3 - Cam 4	37.0%	74.9%	0.72	0.59

TABLE 6

Multi-view GLMB filter runtime on WILDTRACKS and CMC Datasets.

Dataset (Cam)	Frame	No. Obj (avg)	Exec. Time (s/frame)
W.T. (7)	401	20	18.0
CMC1(4)	261	3	0.1
CMC2 (4)	263	10	3.2
CMC3 (4)	263	15	7.9
CMC4 (4)	147	3	0.4

the perfect CLEAR MOT score for MOTA and MOTP. For the medium scenario CMC2, Fig. 2 shows a screenshot of the detections and multi-view GLMB estimates. In this case the multi-view GLMB filter with the proposed detection model manages to maintain consistent tracks and accurate estimates overall. The CLEAR MOT benchmarks for CMC2 show high MOTA and MOTP but with some FNs and FPs. The latter are due to track initiation/termination mismatches with the ground truths, which result in pronounced spikes at the start and end of the OSPA⁽²⁾ plot for CMC2. For the dense scenario CMC3, the proposed algorithm fails when a person is completely occluded in all views. This is illustrated in Fig. 3 where the red bounding boxes denote detections while the yellow bounding boxes indicate people who are undetected in all views. Such situations could cause track termination/switching, which is reflected in Table 4, where CMC3 has the lowest MOTA and MOTP scores.

5.3.7 Runtimes

The runtimes for the multi-view GLMB filter on the WILDTRACKS and CMC datasets are summarized in Table 6. The current implementation is via unoptimized MATLAB code. The reported runtimes appear to be consistent with the computational complexity of the multi-view GLMB algorithm: quadratic in the number of objects and linear in the sum of the number of detections across all cameras. Note that the scenario CMC4 will be discussed in the next subsection.

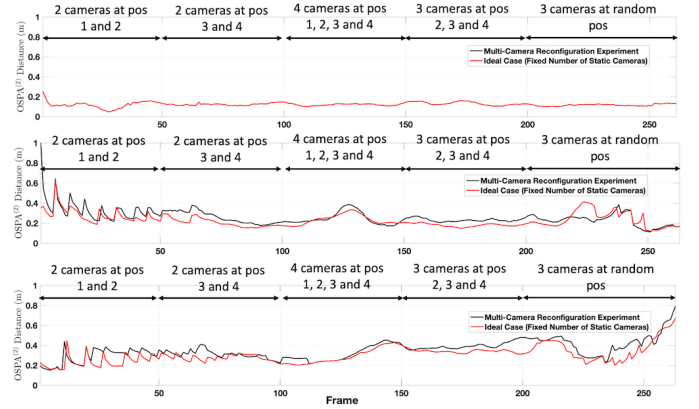


Fig. 5. OSPA⁽²⁾ plots for multi-view GLMB filter tracking results on CMC1, 2 and 3 (top to bottom): black line (for CMC1, is obscured by red line) is the result from the multi-camera reconfiguration experiment while red line is the result from the ideal case where all four cameras are turned on permanently.

5.4 3D Multi-Modal Tracking (CMC4)



Fig. 6. CMC4 Camera 1: YOLOv3 detections (left) and multi-view GLMB estimates (right).

5.4.1 Extension to JMS

We now demonstrate that the proposed framework is further capable of tracking people jumping and falling, by adapting the Jump Markov System (JMS) formulation [49] into the multi-view GLMB filter. A JMS is specified by augmenting the state $\mathbf{x} \in \mathbb{X} \times \mathbb{L}$ with a discrete mode or class $m \in \mathbb{M}$ where \mathbb{M} is the discrete space of modes. The single-object density becomes $p^{(\xi)}(\mathbf{x}, m) = p^{(\xi)}(\mathbf{x}|m)\vartheta^{(\xi)}(m)$. An object with mode m at the current time jumps or transitions to mode m_+ at the next time with Markov transition probability $\vartheta_+(m_+|m)$. The single object transition density for a state \mathbf{x} with mode m to state \mathbf{x}_+ with mode m_+ is denoted by $f_{S,+}(\mathbf{x}_+, m_+|\mathbf{x}, m)$, and state \mathbf{x} with mode m generates measurement $z^{(c)} = (z_p^{(c)}, z_e^{(c)})$ from sensor c according to the single object likelihood $g^{(c)}(z^{(c)}|\mathbf{x}, m)$.

In this experiment, the mode can take on two values i.e., $m \in \{0, 1\}$, where $m = 0$ corresponds to a standing state and $m = 1$ corresponds to a fallen state. The mode transition probabilities are $\vartheta_+(0|0) = 0.7$, $\vartheta_+(1|0) = 0.3$,

TABLE 7

CLEAR MOT benchmark multi-view GLMB filter tracking results on CMC4: \uparrow means higher is better while \downarrow means lower is better, and the asterisk denotes the results from the multi-camera reconfiguration experiment.

Dataset	IDF1 \uparrow	IDP \uparrow	IDR \uparrow	MT \uparrow	PT \downarrow	ML \downarrow	FP \downarrow	FN \downarrow	IDs \downarrow	FM \downarrow	MOTA \uparrow	MOTP \uparrow
CMC4	100.0%	100.0%	100.0%	3	0	0	0	0	0	0	100.0%	100.0%
CMC4*	100.0%	100.0%	100.0%	3	0	0	0	0	0	0	100.0%	100.0%

TABLE 8
CLEAR evaluation for YOLOv3 detector results on CMC4

Dataset	MODA \uparrow	MODP \uparrow	Precision \uparrow	Recall \uparrow
CMC4 - Cam 1	86.8%	82.0%	0.93	0.93
CMC4 - Cam 2	75.2%	79.1%	0.87	0.88
CMC4 - Cam 3	86.7%	84.6%	0.93	0.93
CMC4 - Cam 4	81.5%	82.7%	0.94	0.87

$\vartheta_+(0|1) = 0.6$ and $\vartheta_+(1|1) = 0.4$. It is assumed that the single object transition and likelihood have specific forms

$$f_{S,+}(x_{m+}|x, m) = f_{S,+}^{(m+)}(x_{m+}|x, \ell, m) \delta_{\ell}[\ell_{+}] \vartheta_+(m_{+}|m), \quad (42)$$

$$g^{(c)}(z^{(c)}|x, m) = g_p^{(c)}(z^{(c)}|x) g_e^{(c)}(z_e^{(c)}|m). \quad (43)$$

For a standing object i.e. $m = 0$, the transition and observation models to another standing state i.e. $f_{S,+}^{(0)}(x_{+}|x, \ell, 0)$ and $g_p^{(c)}(z^{(c)}|x, 0)$ respectively, are the same as per the previous subsection. Standing objects typically have a bounding box size ratio (y-axis/x-axis) greater than one, thus the mode dependent likelihood component is chosen as $g_e^{(c)}(z_e^{(c)}|0) = e^{\rho \left(\frac{([0,1]z_e^{(c)})/[1,0]z_e^{(c)}}{1} - 1 \right)}$ for all cameras where $\rho = 4$ is a control parameter.

For a fallen object i.e. $m = 1$, the transition and observation models to another fallen state i.e. $f_{S,+}^{(1)}(x_{+}|x, \ell, 1)$ and $g_p^{(c)}(z^{(c)}|x, 1)$ respectively, are the same as that for standing to standing state except that $v^{(s)} = (0.01, 0.01, 0.01)^T$ and $v_e^{(c)} = (0.0025, 0.01)^T$ for all cameras. Fallen objects typically have a bounding box size ratio (y-axis/x-axis) less than one, thus the mode dependent likelihood component is chosen as $g_e^{(c)}(z_e^{(c)}|1) = e^{-\rho \left(\frac{([0,1]z_e^{(c)})/[1,0]z_e^{(c)}}{1} - 1 \right)}$ for all cameras where $\rho = 4$ is a control parameter.

For a state transition involving a mode switch i.e. standing to fallen or fallen to standing, the transition density $f_{+}^{(1)}(x_{+}|x, \ell, 0)$ or $f_{+}^{(0)}(x_{+}|x, \ell, 1)$ takes on the form (27), with position noise parameterized by $v^{(p)} = (0.0049, 0.0049, 0.0049)^T$, and for the extent (in logarithm) noise by $v^{(s)} = (0.039, 0.039, 0.039)^T$. Notice that the position noise is increased in the case of a mode switch compared to the case of no switching, in order to capture the abrupt change in the size of the ellipsoid during mode switching.

The birth density is an LMB with parameters $P_{B,+}^{(\ell)} = 0.001$ and $f_{B,+}^{(\ell)}(x, 0) = 0.9\mathcal{N}(x; \mu_{B,+}, \Sigma_{B,+})$, $\mu_{B,+} = [2.03 \ 0 \ 0.71 \ 0 \ 0.825 \ 0 \ -1.2 \ -1.2 \ -0.18]^T$, $f_{B,+}^{(\ell)}(x, 1) = 0.1\mathcal{N}(x; \mu_{B,+}, \Sigma_{B,+})$, $\mu_{B,+} = [2.03 \ 0 \ 0.71 \ 0 \ 0.413 \ 0 \ -0.18 \ -0.18 \ -1.2]^T$, $\Sigma_{B,+} = \Sigma_{B,+} = 0.1^2 \mathbf{I}_9$.

5.4.2 CMC4 Dataset and Performance Evaluation

We evaluate the JMS extension of the multi-view GLMB filter on an additional CMC4 dataset, which involves 3

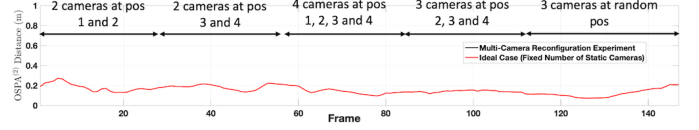


Fig. 7. OSPA⁽²⁾ plot for multi-view GLMB on CMC4: black line (observed by red line) is the result from the multi-camera reconfiguration experiment while red line is the result from the ideal case where all four cameras are turned on permanently.

people walking, jumping and falling throughout the scenario, and is also recorded at 1920x1024 and sampled at 4fps for approximately 1 minute. Table 8 shows the CLEAR evaluation for the YOLOv3 monocular detections for each camera. Similar to the experiments for CMC1-3, we evaluate the performance on CMC4 with a benchmark case where all cameras are always on, as well as the same multi-camera reconfiguration case where cameras are added, removed and repositioned on the fly. Fig. 6 shows a screen shot of the data and estimates for the ideal case. The CLEAR MOT and OSPA⁽²⁾ results for CMC4 are shown in Table 7 and Figure 7 respectively. The runtime for CMC4 is added to Table 6. It can be seen that the JMS variant of the multi-view GLMB filter can obtain both the estimates of trajectories, in addition to correctly capturing the modes of the objects even in the case of camera reconfiguration.

6 CONCLUSION

An online multi-view multi-object filtering algorithm that encapsulates state estimation and track management is proposed. We have shown that our proposed framework resolves the data association problem that arises in the detections from multiple cameras without pre/post-processing. Our method only requires a one-off monocular detector training applied to all cameras. This enables the system uninterrupted in the event of multi-camera extension/reconfiguration (including camera failures), obviating the need of multi-view retraining. Finally, we have demonstrated 3D people tracking with the extension to tracking people jumping and falling. We have also proposed an innovative 3D detection model that has shown to be effective in occlusion handling.

REFERENCES

- [1] F. Poiesi, R. Mazzon, and A. Cavallaro, "Multi-target tracking on confidence maps: An application to people tracking," *Computer Vision and Image Understanding*, vol. 117, no. 10, pp. 1257–1272, 2013.
- [2] R. Hoseinnezhad, B.-N. Vo, B.-T. Vo, and D. Suter, "Visual tracking of numerous targets via multi-bernoulli filtering of image data," *Pattern Recognition*, vol. 45, no. 10, pp. 3625–3635, 2012.
- [3] H. B. Shitrit, J. Berclaz, F. Fleuret, and P. Fua, "Multi-commodity network flow for tracking multiple people," *IEEE transactions on pattern analysis and machine intelligence*, vol. 36, no. 8, pp. 1614–1627, 2014.

- [4] D. Y. Kim, B.-N. Vo, B.-T. Vo, and M. Jeon, "A labeled random finite set online multi-object tracker for video data," *Pattern Recognition*, 2019.
- [5] A. Milan, S. Roth, and K. Schindler, "Continuous energy minimization for multitarget tracking," *IEEE transactions on pattern analysis and machine intelligence*, vol. 36, no. 1, pp. 58–72, 2014.
- [6] X. Wang, E. Türetken, F. Fleuret, and P. Fua, "Tracking interacting objects using intertwined flows," *IEEE transactions on pattern analysis and machine intelligence*, vol. 38, no. 11, pp. 2312–2326, 2016.
- [7] J. Berclaz, F. Fleuret, E. Turetken, and P. Fua, "Multiple object tracking using k-shortest paths optimization," *IEEE transactions on pattern analysis and machine intelligence*, vol. 33, no. 9, pp. 1806–1819, 2011.
- [8] Y. Xu, X. Liu, Y. Liu, and S.-C. Zhu, "Multi-view people tracking via hierarchical trajectory composition," in *Proceedings of the IEEE Conference on Computer Vision and Pattern Recognition*, pp. 4256–4265, 2016.
- [9] M. D. Breitenstein, F. Reichlin, B. Leibe, E. Koller-Meier, and L. Van Gool, "Online multiperson tracking-by-detection from a single, uncalibrated camera," *IEEE transactions on pattern analysis and machine intelligence*, vol. 33, no. 9, pp. 1820–1833, 2010.
- [10] B. Babenko, M.-H. Yang, and S. Belongie, "Robust object tracking with online multiple instance learning," *IEEE transactions on pattern analysis and machine intelligence*, vol. 33, no. 8, pp. 1619–1632, 2010.
- [11] J. F. Henriques, R. Caseiro, P. Martins, and J. Batista, "High-speed tracking with kernelized correlation filters," *IEEE transactions on pattern analysis and machine intelligence*, vol. 37, no. 3, pp. 583–596, 2014.
- [12] P. Peng, Y. Tian, Y. Wang, J. Li, and T. Huang, "Robust multiple cameras pedestrian detection with multi-view Bayesian network," *Pattern Recognition*, vol. 48, no. 5, pp. 1760–1772, 2015.
- [13] S. L. Dockstader and A. M. Tekalp, "Multiple camera fusion for multi-object tracking," in *Multi-Object Tracking, 2001. Proceedings. 2001 IEEE Workshop on*, pp. 95–102, IEEE, 2001.
- [14] F. Fleuret, J. Berclaz, R. Lengagne, and P. Fua, "Multicamera people tracking with a probabilistic occupancy map," *IEEE transactions on pattern analysis and machine intelligence*, vol. 30, no. 2, pp. 267–282, 2008.
- [15] T. Chavdarova *et al.*, "Deep multi-camera people detection," in *2017 16th IEEE International Conference on Machine Learning and Applications (ICMLA)*, pp. 848–853, IEEE, 2017.
- [16] T. Chavdarova, P. Baqué, S. Bouquet, A. Maksai, C. Jose, T. Bagautdinov, L. Lettry, P. Fua, L. Van Gool, and F. Fleuret, "WILDTRACK: A multi-camera HD dataset for dense unscripted pedestrian detection," in *Proceedings of the IEEE Conference on Computer Vision and Pattern Recognition*, pp. 5030–5039, 2018.
- [17] P. Baqué, F. Fleuret, and P. Fua, "Deep occlusion reasoning for multi-camera multi-target detection," in *Proceedings of the IEEE International Conference on Computer Vision*, pp. 271–279, 2017.
- [18] J. Domke, "Learning graphical model parameters with approximate marginal inference," *IEEE transactions on pattern analysis and machine intelligence*, vol. 35, no. 10, pp. 2454–2467, 2013.
- [19] B.-N. Vo, B.-T. Vo, and M. Beard, "Multi-sensor multi-object tracking with the generalized labeled multi-Bernoulli filter," *IEEE Transactions on Signal Processing*, 2019.
- [20] A. Krizhevsky, I. Sutskever, and G. E. Hinton, "Imagenet classification with deep convolutional neural networks," in *Advances in neural information processing systems*, pp. 1097–1105, 2012.
- [21] R. Girshick, "Fast R-CNN," in *Proceedings of the IEEE international conference on computer vision*, pp. 1440–1448, 2015.
- [22] S. Ren, K. He, R. Girshick, and J. Sun, "Faster R-CNN: Towards real-time object detection with region proposal networks," in *Advances in neural information processing systems*, pp. 91–99, 2015.
- [23] J. Redmon and A. Farhadi, "YOLO9000: better, faster, stronger," in *Proceedings of the IEEE conference on computer vision and pattern recognition*, pp. 7263–7271, 2017.
- [24] J. Redmon, S. Divvala, R. Girshick, and A. Farhadi, "You only look once: Unified, real-time object detection," in *Proceedings of the IEEE conference on computer vision and pattern recognition*, pp. 779–788, 2016.
- [25] X. Zhao, H. Jia, and Y. Ni, "A novel three-dimensional object detection with the modified you only look once method," *International Journal of Advanced Robotic Systems*, vol. 15, no. 2, p. 1729881418765507, 2018.
- [26] M. Andriluka, S. Roth, and B. Schiele, "People-tracking-by-detection and people-detection-by-tracking," in *2008 IEEE Conference on computer vision and pattern recognition*, pp. 1–8, IEEE, 2008.
- [27] A. W. Smeulders, D. M. Chu, R. Cucchiara, S. Calderara, A. Dehghan, and M. Shah, "Visual tracking: An experimental survey," *IEEE transactions on pattern analysis and machine intelligence*, vol. 36, no. 7, pp. 1442–1468, 2013.
- [28] R. P. Mahler, "Multitarget Bayes filtering via first-order multitarget moments," *IEEE Transactions on Aerospace and Electronic systems*, vol. 39, no. 4, pp. 1152–1178, 2003.
- [29] R. P. Mahler, *Statistical multisource-multitarget information fusion*. Artech House, Inc., 2007.
- [30] R. P. Mahler, *Advances in statistical multisource-multitarget information fusion*. Artech House, 2014.
- [31] E. Maggio, M. Taj, and A. Cavallaro, "Efficient multitarget visual tracking using random finite sets," *IEEE Transactions on Circuits and Systems for Video Technology*, vol. 18, no. 8, pp. 1016–1027, 2008.
- [32] B.-T. Vo and B.-N. Vo, "Labeled random finite sets and multi-object conjugate priors," *IEEE Transactions on Signal Processing*, vol. 61, no. 13, pp. 3460–3475, 2013.
- [33] E. Ristani, F. Solera, R. Zou, R. Cucchiara, and C. Tomasi, "Performance measures and a data set for multi-target, multi-camera tracking," in *European Conference on Computer Vision*, pp. 17–35, Springer, 2016.
- [34] J. Ferryman and A. Shahrokni, "Pets2009: Dataset and challenge," in *2009 Twelfth IEEE International Workshop on Performance Evaluation of Tracking and Surveillance*, pp. 1–6, IEEE, 2009.
- [35] X. Alameda-Pineda, J. Staiano, R. Subramanian, L. Batrinca, E. Ricci, B. Lepri, O. Lanz, and N. Sebe, "Salsa: A novel dataset for multimodal group behavior analysis," *IEEE Transactions on Pattern Analysis and Machine Intelligence*, vol. 38, no. 8, pp. 1707–1720, 2015.
- [36] B.-N. Vo, S. Singh, and A. Doucet, "Sequential Monte Carlo methods for multitarget filtering with random finite sets," *IEEE Transactions on Aerospace and electronic systems*, vol. 41, no. 4, pp. 1224–1245, 2005.
- [37] B.-N. Vo, B.-T. Vo, and H. G. Hoang, "An efficient implementation of the generalized labeled multi-Bernoulli filter," *IEEE Transactions on Signal Processing*, vol. 65, no. 8, pp. 1975–1987, 2017.
- [38] M. Beard, B.-T. Vo, and B.-N. Vo, "Bayesian multi-target tracking with merged measurements using labelled random finite sets," *IEEE Trans. Signal Processing*, vol. 63, no. 6, pp. 1433–1447, 2015.
- [39] Z. Zhang, "A flexible new technique for camera calibration," *IEEE Transactions on pattern analysis and machine intelligence*, vol. 22, no. 11, pp. 1330–1334, 2000.
- [40] T. T. D. Nguyen and D. Y. Kim, "GLMB tracker with partial smoothing," *Sensors*, vol. 19, no. 20, p. 4419, 2019.
- [41] P. Schneider and D. H. Eberly, *Geometric tools for computer graphics*. Elsevier, 2002.
- [42] R. Hartley and A. Zisserman, *Multiple view geometry in computer vision*. Cambridge university press, 2003.
- [43] L. Leal-Taixé, A. Milan, I. Reid, S. Roth, and K. Schindler, "Motchallenge 2015: Towards a benchmark for multi-target tracking," *arXiv preprint arXiv:1504.01942*, 2015.
- [44] R. Kasturi, D. Goldgof, P. Soundararajan, V. Manohar, J. Garofolo, R. Bowers, M. Boonstra, V. Korzhova, and J. Zhang, "Framework for performance evaluation of face, text, and vehicle detection and tracking in video: Data, metrics, and protocol," *IEEE transactions on Pattern Analysis and Machine intelligence*, vol. 31, no. 2, pp. 319–336, 2008.
- [45] M. Beard, B. T. Vo, and B.-N. Vo, "OSPA (2): Using the OSPA metric to evaluate multi-target tracking performance," in *Control, Automation and Information Sciences (ICCAIS), 2017 International Conference on*, pp. 86–91, IEEE, 2017.
- [46] D. Schuhmacher, B.-T. Vo, and B.-N. Vo, "A consistent metric for performance evaluation of multi-object filters," *IEEE Transactions on Signal Processing*, vol. 56, no. 8, pp. 3447–3457, 2008.
- [47] M. Beard, B. T. Vo, and B.-N. Vo, "Performance evaluation for large-scale multi-target tracking algorithms," in *2018 21st International Conference on Information Fusion (FUSION)*, pp. 1–5, IEEE, 2018.
- [48] S. Reuter, B.-T. Vo, B.-N. Vo, and K. Dietmayer, "The labeled multi-Bernoulli filter," *IEEE Transactions on Signal Processing*, vol. 62, no. 12, pp. 3246–3260, 2014.
- [49] Y. G. Punchihewa, B.-T. Vo, B.-N. Vo, and D. Y. Kim, "Multiple object tracking in unknown backgrounds with labeled random finite sets," *IEEE Transactions on Signal Processing*, vol. 66, no. 11, pp. 3040–3055, 2018.

7 APPENDIX

7.1 Gibbs Sampler for Multi-sensor GLMB Truncation

Gibbs sampling from a stationary distribution involves constructing a Markov chain where the transition from the current state $\gamma = (\gamma_1, \dots, \gamma_P)$ to the next state $\gamma' = (\gamma'_1, \dots, \gamma'_P)$ can be obtained by sampling sequentially from the conditionals $\pi_n(\gamma'_n | \gamma'_{1:n-1}, \gamma_{n+1:P})$ for $n = 1, \dots, P$.

For the stationary distribution (41), the n -th conditional is given by [19]

$$\pi_n(\gamma_{+,n} | \gamma_{+, \bar{n}}) \propto \vartheta_n(\gamma_{+,n}) \prod_{c=1}^C \beta_n^{(c)}(\gamma_{+,n}^{(c)} | \gamma_{+, \bar{n}}^{(c)}), \quad (44)$$

where $\bar{n} = \{1 : P\} - \{n\}$, $\gamma_{+, \bar{n}} = (\gamma_{+,1:n-1}, \gamma_{+,n+1:P})$, and

$$\beta_n^{(c)}(\gamma_{+,n}^{(c)} | \gamma_{+, \bar{n}}^{(c)}) = 1 - 1_{\{1:|Z^{(c)}|\} \cap \{\gamma_{+,1:n-1}^{(c)}, \gamma_{+,n+1:P}^{(c)}\}}(\gamma_{+,n}^{(c)}). \quad (45)$$

Choosing $\vartheta_n(\gamma_{+,n}) = \omega_{\mathbf{X}_+^{(\xi, \gamma_{+,n})}}(\ell_n)$ results in a complexity that is linear in the product of total number of detections across all sensors [19]. Such complexity is not feasible for applications involving many cameras and detections.

A more efficient alternative is

$$\vartheta_n(j^{(1:C)}) = \begin{cases} \eta_n^{(1)}(-1), & j^{(1)}, \dots, j^{(C)} = -1 \\ \prod_{c=1}^C \eta_n^{(c)}(j^{(c)}), & j^{(1:C)} \succeq 0 \end{cases}, \quad (46)$$

where \succeq denotes a component-wise inequality and

$$\eta_n^{(c)}(j^{(c)}) \triangleq \begin{cases} (1 - \bar{P}_S^{(\xi)}(\ell_n))^{\delta_1[c]}, & \ell_n \in I, j^{(c)} < 0 \\ (\bar{P}_S^{(\xi)}(\ell_n))^{\delta_1[c]} \bar{\psi}_{Z_+^{(c)}, \mathbf{X}_+^{(\xi, \mathcal{L}(\gamma_{+,n})}}(\ell_n), \ell_n \in I, j^{(c)} \geq 0 \\ (1 - P_{B,+}(\ell_n))^{\delta_1[c]}, & \ell_n \in \mathbb{B}_+, j^{(c)} < 0 \\ (P_{B,+}(\ell_n))^{\delta_1[c]} \bar{\psi}_{Z_+^{(c)}, \mathbf{X}_+^{(\xi, \mathcal{L}(\gamma_{+,n})}}(\ell_n), \ell_n \in \mathbb{B}_+, j^{(c)} \geq 0 \end{cases}, \quad (47)$$

$$\bar{\psi}_{Z_+^{(c)}, \mathbf{X}_+^{(\xi, \mathcal{L}(\gamma_{+,n})}}(\ell_n) = \left\langle \bar{p}_+^{(\xi)}(\cdot, \ell_n), \psi_{Z_+^{(c)}, \mathbf{X}_+^{(\xi, \mathcal{L}(\gamma_{+,n})}}(\cdot, \ell_n) \right\rangle, \quad (48)$$

$$\bar{p}_+^{(\xi)}(x_+, \ell_n) = 1_{\mathbb{L}}(\ell_n) \frac{\left\langle P_S(\cdot, \ell_n) f_{S,+}(x_+ | \cdot, \ell_n), p^{(\xi)}(\cdot, \ell_n) \right\rangle}{\bar{P}_S^{(\xi)}(\ell)} + 1_{\mathbb{B}_+}(\ell_n) f_{B,+}(x_+, \ell_n), \quad (49)$$

This choice of ϑ_n results in the so-called Minimally-Markovian (MM) Gibbs sampler with a complexity that is linear in the sum of total number of detections (scalable) across all sensors, and quadratic in the number of components. Details of this strategy can be found in [19]. The pseudocode for this MM-Gibbs sampler is summarized in Algorithm 1.

Algorithm 1 MM-Gibbs(\cdot)

Inputs: $T, C, \gamma^{(1)} = [\gamma_n^{(1,c)}], \vartheta = \{[\eta_n^{(c)}(j^{(c)})]\}_{c=1}^C$
Outputs: $\gamma^{(1)}, \dots, \gamma^{(T)}$

```

P = size( $\vartheta$ , 1)
for c = 1 : C
    M(c) = size( $\vartheta^{(c)}$ , 2) - 2, q(c) = [0 : M(c)]
end for
for n = 1 : P
    for c = 1 : C
         $\Upsilon_n^{(c)} = \sum_{j^{(c)}=0}^{M^{(c)}} \beta_n^{(c)}(j^{(c)} | \gamma_{\bar{n}}^{(c)}) \vartheta_n^{(c)}(j^{(c)})$ 
    end
    Compute  $\Omega_n = \frac{\prod_{c=1}^C \Upsilon_n^{(c)}}{\prod_{c=1}^C \vartheta_n^{(c)}(-1) + \prod_{c=1}^C \Upsilon_n^{(c)}}$ ,  $\bar{\Omega}_n = 1 - \Omega_n$ 
end for
for t = 2 : T
     $\phi^{(t)} = []$ 
    for n = 1 : P
         $i_n \sim \text{Categorical}([+, -], [\Omega_n, \bar{\Omega}_n])$ 
        if  $i_n = +$ 
            for c = 1 : C
                for j(c) = 0 : M(c)
                     $p_n^{(c)}(j^{(c)}) = \vartheta_n^{(c)}(j^{(c)}) \beta_n^{(c)}(j^{(c)} | \phi_{1:n-1}^{(t,c)}, \gamma_{n+1:P}^{(t-1,c)})$ 
                end for
                 $\phi_n^{(t,c)} \sim \text{Categorical}(q^{(c)}, p_n^{(c)})$ 
            end for
             $\phi_n^{(t)} = [\phi_n^{(t,c)}]_{c=1}^C$ 
        else if
             $\phi_n^{(t)} = -1 * \text{ones}(1, C)$ 
        end if
         $\phi^{(t)} = [\phi^{(t)}; \phi_n^{(t)}]$ 
    end for
     $\gamma^{(t)} = \phi^{(t)}$ 
end for

```

7.2 Pseudocode for Multi-view GLMB filter

Suppose that the current GLMB filtering density are enumerated as $\{(I^{(h)}, w^{(h)}, p^{(h)})\}_{h=1}^H$ where $w^{(h)} \triangleq w^{(\xi^{(h)})}, p^{(h)} \triangleq p^{(\xi^{(h)})}$. The GLMB recursion (17) computes the components of the GLMB filtering density at the next time. Each component h requires pre-computation of the $p^{(h)}$ -predicted value $\mathbf{X}_+^{(h, \mathbb{B}_+ \cup I^{(h)})} \triangleq \mathbf{X}_+^{(\xi^{(h)}, \mathbb{B}_+ \cup I^{(h)})}$ according to (25). The $p^{(h)}$ -predicted values $\mathbf{x}^{(h, \ell)} \in \mathbf{X}_+^{(h, \mathbb{B}_+ \cup I^{(h)})}$, are then used to compute approximate detection probabilities $P_D^{(c)}(\mathbf{x}^{(h, \ell)}; \mathbf{X}_+^{(h, \mathbb{B}_+ \cup I^{(h)})})$ via (10) and approximate survival probabilities $P_S(\mathbf{x}^{(h, \ell)})$ via (30), which are needed for the computation of $\{\eta^{(h,c)}\}_{c=1}^C$. We adopt the MM-Gibbs(\cdot) routine in Algorithm 1 to draw $T_+^{(h)}$ samples $(\gamma_+^{(h,t)})$. Recall that the term $\beta_n^{(c)}(j^{(c)} | \phi_{1:n-1}^{(t,c)}, \gamma_{n+1:P}^{(t-1,c)})$ (45), ensures the positive 1-1 mapping property in $\gamma^{(h,t)}$. Given a particular $\gamma_+^{(h,t)} = \{\gamma_+^{(h,t,c)}\}_{c=1}^C$ and $I_+^{(h,t)} = \mathcal{L}(\gamma_+^{(h,t)})$, it is necessary to re-compute the $p^{(h)}$ -predicted values $\mathbf{X}_+^{(h, I_+^{(h,t)})} = \{\mathbf{x}^{(h,t, \ell)} : \ell \in I_+^{(h,t)}\}$ and the approximate detection probabilities $P_D^{(c)}(\mathbf{x}^{(h,t, \ell)}; \mathbf{X}_+^{(h, I_+^{(h,t)})})$, in order to update the new $w_+^{(h,t)}$ and $p_+^{(h,t)} = p^{(h, \gamma_+^{(h,t)})}$. The pseudocode is summarized

in Algorithm 2 wherein $\text{Unique}(\cdot)$ refers to the built-in MATLAB function.

Algorithm 2 Multi-view GLMB Filter

Global Input: $\left\{ \left(I^{(h)}, w^{(h)}, p^{(h)} \right) \right\}_{h=1}^H, Z_+, H_+^{\max}$

Global Input: $\left\{ \left(P_{B,+}^{(\ell)}, f_{B,+}^{(\ell)} \right) \right\}_{\ell \in \mathbb{B}_+}, f_{S,+}(\cdot), b(\cdot)$

Global Input: $\left\{ \left(\kappa^{(c)}, P_D^{(c)}(\cdot), g^{(c)}(\cdot|\cdot) \right) \right\}_{c=1}^C$

Output: $\left\{ \left(I_+^{(h_+)}, w_+^{(h_+)}, p_{Z_+, \mathbf{X}_+}^{(h_+)} \right) \right\}_{h_+=1}^{H_+}$

Sample counts $\left[T_+^{(h)} \right]_{h=1}^H$ from multinomial distribution

with parameters H_+^{\max} trials and weights $\left[w^{(h)} \right]_{h=1}^H$

for $h \in \{1 : H\}$

$\left[\left(\mathbf{x}^{(h,\ell)}, P_S^{(h,\ell)}, P_D^{(h,\ell,c)} \right) \right]_{\substack{\ell \in \mathbb{B}_+ \uplus I^{(h)} \\ c \in \{1:C\}}} = \text{CalcPsPd}(p^{(h)}, \mathbb{B}_+ \uplus I^{(h)})$

Initialize $\gamma_+^{(h,1)}$

Compute $\vartheta^{(h)} = \{\eta^{(h,c)}\}_{c=1}^C$ using (47)

$\left\{ \gamma_+^{(h,t)} \right\}_{t=1}^{\tilde{T}^{(h)}} = \text{Unique}(\text{MM-Gibbs}(T_+^{(h)}, C, \gamma_+^{(h,1)}, \vartheta^{(h)}))$

for $t \in \{1 : \tilde{T}^{(h)}\}$

Compute

$I_+^{(h,t)} = \left\{ \ell_n \in \mathbb{B}_+ \uplus I^{(h)} : \gamma_+^{(h,t)}(\ell_n) \geq 0 \right\}$
 $\left[\left(\mathbf{x}_+^{(h,t,\ell)}, P_S^{(h,t,\ell)}, P_D^{(h,t,\ell,c)} \right) \right]_{\substack{\ell \in I_+^{(h,t)} \\ c \in \{1:C\}}} = \text{CalcPsPd}(p^{(h)}, I_+^{(h,t)})$

$w_+^{(h,t)} \propto w^{(h)} \prod_{n=1}^{|\mathbb{B}_+ \uplus I^{(h)}|} \prod_{c=1}^C \eta_n^{(h,c)} \left(\gamma_+^{(h,t,c)}(\ell_n) \right)$ using (47)

$p_{Z_+, \mathbf{X}_+}^{(h, \gamma_+^{(h,t)})}$ using (19)

end for

end for

$\left(\left\{ \left(I_+^{(h_+)}, p_{Z_+, \mathbf{X}_+}^{(h_+)} \right) \right\}_{h_+=1}^{H_+}, \sim, [U_{h,t}] \right)$
 $= \text{Unique} \left(\left\{ \left(I_+^{(h,t)}, p_{Z_+, \mathbf{X}_+}^{(h, \gamma_+^{(h,t)})} \right) \right\}_{(h,t)=(1,1)}^{(H, \tilde{T}^{(h)})} \right)$

for $h_+ \in \{1 : H_+\}$

$w_+^{(h_+)} = \sum_{h,t: U_{h,t}=h_+} w_+^{(h,t)}$

end for

Normalize weights $\left\{ w_+^{(h_+)} \right\}_{h_+=1}^{H_+}$

Algorithm 3 CalcPsPd(\cdot)

Input: $p^{(h)}, J \subseteq \mathbb{L}_+$

Output: $\left[\left(\mathbf{x}^{(h,\ell)}, P_S^{(h,\ell)}, P_D^{(h,\ell,c)} \right) \right]_{\substack{\ell \in J \\ c \in \{1:C\}}}$

Compute $\mathbf{X}^{(h,J)} = \left\{ \mathbf{x}^{(h,\ell)} : \ell \in J \right\}$ with $p^{(h)}$ via (25)

Compute $P_S^{(h,\ell)} := P_S(\mathbf{x}^{(h,\ell)})$ for $\mathbf{x}^{(h,\ell)} \in \mathbf{X}^{(h,J)}$ via (30)

for $c \in \{1 : C\}$

Compute $P_D^{(h,\ell,c)} := P_D^{(c)}(\mathbf{x}^{(h,\ell)}; \mathbf{X}^{(h,J)})$
for $\mathbf{x}^{(h,\ell)} \in \mathbf{X}^{(h,J)}$ via (10)

end for
